(Received 5 July 2025, Accepted 22 September 2025, Scheduled 23 October 2025)

High Selectivity Tri-Coupled Line Bandpass Filter Based on Even- and Odd-Mode Impedance Modeling

Moretadha J. Kadhom*

University of Baghdad, Baghdad, Iraq

ABSTRACT: This research introduces a compact and highly selective tri-coupled line microstrip bandpass filter. The design features a narrow capacitive gap positioned at the midline to disrupt symmetry and facilitate bandpass functionality, as predicted through an even- and odd-mode image impedance framework. The split at the midline generates two modal capacitances (C_{gg}, C_{gb}), which influence Re (Z_i) and, in conjunction with geometric coupling, determine the passband and roll-off characteristics. Closed-form relationships for microstrip design are utilized to compute line widths and electrical lengths. A systematic parametric analysis demonstrates how the gap and interline spacing impact the fractional bandwidth and the steepness of the transition. Additionally, a substrate survey across dielectric constants ranging from 2 to 12.2 quantifies the trade-off between footprint and selectivity, indicating an area reduction of up to approximately 86% at higher dielectric constants. The selectivity is further enhanced by incorporating auxiliary shunt open stubs that introduce transmission zeros near the edges without necessitating additional resonator sections. A prototype fabricated on an FR-4 substrate operating at 2.4 GHz confirms the theoretical model: the measured $|S_{21}|$ exhibits an insertion loss of approximately 0.58 dB, a fractional bandwidth at 3 dB of approximately 37. 3%, a shape factor of 1.3, and two prominent TZs near 1.7 GHz and 3.1 GHz with rejection levels of 4852 dB. Furthermore, the upper stopband maintains $|S_{21}| < -35$ dB within the frequency range of 3.10 to 3.20 GHz. These findings substantiate that a single TCL section, featuring a central gap and open stubs, can achieve sharp roll-off and low insertion loss while maintaining minimal layout complexity and enabling straightforward tuning on low-cost printed circuit board materials.

1. INTRODUCTION

Microwave filters are essential parts of modern communication and radar systems because they help maintain signal quality and ensure that the system works optimally. Over time, many different approaches have been developed to design these filters, with one of the main methods being the insertion loss technique, where the filter is initially modeled using lumped elements and then transformed into distributed structures for practical use [1, 2]. Alternatively, direct methods using distributed elements like transmission lines and waveguides are utilized to create filters based on their inherent electromagnetic properties, providing improved performance [3, 4]. Microstrip technology, known for its planar design, easy manufacturing, simple integration with other circuit components, compatibility with printed circuit board (PCB) processes, and cost-efficiency, has become widely used in modern microwave filter designs, especially where compactness and integration into complex RF systems are essential [5–7]. Coupled line (CL) microstrip filters, in particular, have gained significant interest because they enable flexible control over frequency response through even- and odd-mode analysis, providing versatile options such as low-pass (LPF), high-pass (HPF), bandpass (BPF), and stopband filters (SBF) [8–10]. However, conventional single-section CL filters often face significant limitations because they typically cannot meet the stringent selectivity, narrow BP features, and bandwidth requirements required by modern high-performance communication systems. These inherent limitations call for the exploration and development of more advanced and sophisticated topologies, such as multi-section filters and structurally modified CL configurations, to meet the increasingly demanding specifications and improve overall filter performance [11, 12]. Extensive research has been dedicated to enhancing the performance of conventional complementary least filter designs. Some of the methods explored include adding corrugations [13, 14], using floating strip conductors on substrates [15–17], and applying inductive compensations [18–20]. Advanced analytical models based on even- and odd-mode impedances have significantly enhanced CL filter designs, enabling more accurate predictions and improved frequency responses. The coupling matrix decomposition method, for instance, directly links immittance inverter coefficients to coupling coefficients under non-resonating conditions, enabling filters to be efficiently broken down into sub-filters. This decomposition makes the design and optimization process easier by systematically handling complex interactions within CL structures [21]. Furthermore, suspended substrate stripline BPFs employing source-load coupling structures benefit significantly from a combined lumped-element and full-wave mixed approach, which enhances bandwidth through strategically excited loaded resonances and facilitates rapid parameter optimization between equivalent circuits and physical implementations [22]. Additionally, ultra-wideband BPFs that use matching lines and interdigital fil-

* Corresponding author: Moretadha J. Kadhom (moretadha@coeng.uobaghdad.edu.iq).

ters with closely coupled resonators have shown impressive performance gains. By incorporating $\lambda/4$ inverter lines and smart impedance matching techniques, these designs deliver excellent matching, wide BP coverage, and strong signal rejection. This success highlights how advanced analytical modeling significantly improves modern CL filter designs [23]. In CL filters, the main coupling occurs between neighboring lines, which significantly affects how the modes behave and enables better control of the BP performance through careful design adjustments [24, 25]. However, symmetric CL structures naturally behave like all-pass filters, so they require additional design changes to achieve the desired frequency selectivity. To address this, microstrip BPF baluns using double-sided parallel-strip lines with a novel coupling approach have been developed. These baluns show excellent frequency selectivity and maintain stable out-of-phase performance [26]. Moreover, cascaded three-conductor CL filters with apertures in the ground plane effectively convert symmetrical three-conductor structures into simpler two-conductor CLs. This helps better control the even- and odd-mode signals and boosts filter design flexibility by using defected ground structures (DGSs), which greatly improve the stopband performance [27]. Additionally, multilayer CL BPFs based on conductor-backed coplanar transmission lines have been analytically characterized, demonstrating improved radiation and propagation properties. These designs reduce radiation losses and increase power handling by carefully placing dielectric materials in a multilayer setup, further proving the effectiveness of such structural innovations in enhancing CL BPF performance [28]. Balanced BPFs are realized using parallel-coupled microstrip lines augmented with open/shorted loaded stubs, forming a compact balanced topology [29]. Coupled-line sections remain a flexible scaffold for microstrip BPFs: in quasi-absorptive architectures, a reflective-type coupled-line bandpass core is paired with absorptive (resistively loaded) stubs, so the absorptive path governs usable bandwidth, while the coupled-line section sets out-of-band roll-off; the overall order is then scaled by cascading additional coupled-line sections [30]. In dual-band topologies, three-line coupling offers an extensive baseline response, while a loaded asymmetric two-coupled-line resonator introduces transmission zeros (TZs) to delineate two passbands, illustrating how geometry and loading influence the placement of passbands [31]. Interdigital implementations explicitly rely on coupled/tapped lines and extend tuning by embedding folded-spiral stepped-impedance resonators to achieve large, adjustable fractional bandwidth (FBW) while preserving low loss [32]. A dual-band design is presented that utilizes coupled microstrip rings, resulting in sharp roll-off and strong signal rejection in the stopbands. Implementations on common substrates, such as alumina and FR4, have demonstrated that advanced CL filter designs can significantly enhance performance [33]. A coupled-line with step impedance resonator (SIR) topology achieves a multiband band-stop response; tuning gives multimode selectivity and enhanced rejection, validated by microstrip prototypes [34]. Dual-mode dual-band BPF employs asymmetrical TZs and shared coupled-feed lines, enabling compact structure and enhanced cutoff rejection performance [35]. An L-band composite right/left-handed transmission line BPF cascades an interdigitated coupled-line high-pass module with a C-type low-pass resonator; loading a complementary split-ring resonator defected ground introduces an out-of-band TZ and yields a compact, low-loss, selective design [36]. A high-selectivity BPF is formed by two merged microstrip ring resonators sharing a common section; even/odd-mode analysis predicts multiple TZs, and a fabricated prototype verifies the approach [37]. Balanced BPF using a loop-type microstrip resonator with shorted/opened stubs, fed by balanced coupled lines, suppresses common-mode via modal separation, asymmetric port coupling, and grounded-resistor dissipation, demonstrated by a 2.4 GHz prototype [38]. Coupled-resonator BPFs can be synthesized by extracting circuit parameters for parallel- and end-coupled transverse electromagnetic (TEM) resonators directly from a coupling matrix, enabling controlled couplings before EM tuning [39]. Multi-coupled line filters, combined with stub-loaded stepped-impedance resonators, enable the construction of compact quad-band filters with separate bandpass frequencies, making them ideal for 5G networks [40]. Filters using stub-loaded uniform impedance resonators with L-shaped feeds deliver dual-band operation while reducing unwanted signals [41]. Dual-mode coupling resonators are utilized to introduce TZs near the BP, thereby enhancing filter performance and selectivity [42]. Compact reconfigurable filters using $\lambda/4$ stubs can support multiple bandpass responses and create numerous TZs, making them ideal for ultra-wideband applications [43]. Miniaturized ultra-wideband filters based on multi-stub-loaded stepped impedance ring resonators deliver wide fractional bandwidths and low insertion losses [44]. Uniform transmission line filters loaded with $\lambda/4$ stubs provide dual-notch features with low insertion loss and broad fractional bandwidths, meeting the needs of wireless communication systems [45]. Edge-coupled microstrip filters loaded with split-ring resonators (SRRs) demonstrate simultaneous BP filtering and displacement sensing capabilities [46]. For sub-6 GHz 5G, compact parallel-coupled microstrip filters provide low signal loss, reduce noise, and are compatible with affordable FR-4 substrates [47]. Filtering switches made from optimized CLs and PIN diodes switch between filtering and shutdown modes, offering high selectivity and blocking unwanted signals [48]. Using inductively compensated CL resonators helps shrink $\lambda/4$ lines without introducing losses, as supported by solid design and testing [49]. Dual and wideband filters that combine CLs with tri-stepped impedance stubs offer flexible bandwidth control and strong selectivity, making them suitable for GSM and GPS systems [50]. Compact filters with open or shortened CL sections and SIRs provide stable and adjustable bandwidths with minimal loss [51]. A sub-6-GHz BPF was synthesized using chained even- and odd-mode admittance polynomials; fabrication sensitivity was reduced relative to Chebyshev designs; response was preserved, and a compact prototype was implemented and measured to validate the tolerance-friendly method and in-band performance [52]. A dual-band absorptive BPF exhibiting reflectionless behavior across all frequencies and improved suppression in the upper band was introduced. This design integrates a ring resonator with coupled lines and absorptive branches [53]. A compact BPF employing three terminated coupled lines, loaded with open and short stubs, was analyzed

through even-odd mode analysis and was verified to attain high selectivity [54]. A single-ended and balanced BPF employing three pairs of coupled lines with stepped-impedance stubs was analyzed and prototyped, demonstrating sharp roll-off characteristics and TZs [55]. A highly compact BPF employing a capacitor-loaded one-eighth-wavelength three-line coupled configuration has been proposed. Capacitors are utilized to control differential-mode poles and zeros, as well as common-mode (CM) zeros, thereby facilitating a wideband response, suppression of common-mode signals, reduced physical dimensions, and minimized insertion loss [56]. Coupled-line and T-shaped microstrip structures were analyzed to realize quasi-reflectionless BPF and SBF; duplexer architectures and absorption channels were employed, and prototypes were fabricated and measured, validating bandwidth control for single- and two-port implementations [57]. A direct synthesis method for wideband filtering switches was developed through the integration of PIN diodes into resonators. Prototypes with fractional bandwidths of 30% and 50% were fabricated and experimentally validated [58]. Gap-fed or gap-coupled microstrip bandpass filters typically employ a small capacitive gap between separate resonators or between a feed line and a resonator. This gap functions as a J-inverter, effectively regulating the inter-resonator coupling and bandwidth. Notable examples include capacitive gap-coupled filters designed using image-impedance methods, along with practical microstrip implementations that deliberately treat the gap as an admittance inverter. Additionally, ring-resonator filters are frequently excited through a capacitive gap that affects external coupling [59–62]. In contrast, the current work introduces a capacitive gap within a single tri-coupled-line (TCL) section, which separates the midline conductor. By modifying the current path through the coupled-line network alongside the outer rails, this design creates internal modal capacitances, rendering the real part of the image impedance frequency-dependent. Consequently, this approach converts an otherwise all-pass TCL into a compact, tunable bandpass section, eliminating the need for inter-resonator inverters or gap-fed resonators. This study introduces a single-section tri-coupled line characterized by a central gap along its midline. The presence of the gap disrupts symmetry and results in the formation of two modal capacitances (C_{gg} and C_{gb}), thereby altering the image impedance to enable a compact and tunable bandpass filter (BPF). The integration of open stubs further improves impedance matching and enhances selectivity. Table 1 provides a comparative analysis of selectivity mechanisms in coupled-line (CL) filters and related topologies, situating the TCL BPF within this context.

2. PROPERTIES OF A COUPLED LINE FILTER

At their core, the CL filters can be thought of as two-port transmission line networks, which we analyze using a set of parameters known as ABCD parameters. These parameters describe how voltages and currents behave at the input and output ports of the filter, enabling the estimation of its characteristics, such as input impedance and signal transmission. Consider a two-port transmission line network shown in Fig. 1. This network

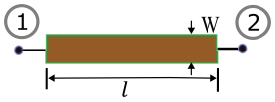

FIGURE 1. Geometry of a two-port microstrip line.

is characterized by its ABCD parameters [57–59].

$$\begin{bmatrix} A & B \\ C & D \end{bmatrix} = \begin{bmatrix} \cos(\beta l) & jZ_0 \sin(\beta l) \\ \frac{j \sin(\beta l)}{Z_0} & \cos(\beta l) \end{bmatrix} \tag{1}$$

where Z_0, l, and β represent the characteristic impedance of the transmission line, physical length, and phase constant, respectively, while $\theta = \beta l$ denotes the electrical length. The derived image impedance Z_i from the ABCD parameters can provide the initial insight into any filter type: LPF, HPF, BPF, SBF, all-pass, or all-stop filters, as [66].

$$Z_i = \sqrt{\frac{AB}{CD}} = Z_0 \tag{2}$$

This impedance represents the input impedance when the output is terminated with the same impedance. In the case of the single transmission line structure, substituting the ABCD parameters into the image impedance equation reveals that Z_i remains real and constant across all frequencies. This indicates that the structure behaves as an all-pass filter. On the other hand, the transmission coefficient, or S_{21} parameter, is a primary parameter for examining the filter frequency response. It can be calculated from the ABCD parameters as [58, 61]

$$S_{21} = \frac{2}{A + B/Z_0 + CZ_0 + D} \tag{3}$$

The values of Equation (1) can be substituted into Equation (3) to obtain $S_{21} = \cos(\beta l) - j \sin(\beta l)$, and this quantity is written in polar form as $S_{21} = |S_{21}| e^{-j\beta l}$ and $|S_{21}|$ is unity at all frequencies. This reaffirms the all-pass behavior, where only the phase varies with frequency, not the amplitude.

| The coupling between adjacent lines produces the desired filtering behavior in practical microwave filter design, particularly with microstrip structures. The limitations of a single-line model (all-pass) are addressed by adding a dual-coupled line (DCL) section, which introduces modal dispersion and differential propagation paths. Selective filtering is achieved by designing these sections, which highlight the differences between even- and odd-mode propagations. The following section further explains these principles, introducing a tri-coupled line (TCL) section and examining how structural modifications (e.g., gaps) impact performance.

2.1. Dual-Coupled Line Filters

In microwave filter design, the behavior of the DCL is foundational for developing advanced filtering structures. These lines are often realized as microstrip lines on a PCB, where electromagnetic coupling between adjacent lines enables BP behavior. The study of such structures benefits from even- and odd-mode analysis, which separates the composite electromagnetic fields

TABLE 1. Qualitative comparison of selectivity mechanisms.

Approach	Selectivity mechanism	complexity	Tuning parameters	Notes
Proposed TCL & insertion gap (current study)	Modal C_{gg} and C_{gb} reshape Re(Z_i)	Low	Length/gap	Enhanced tunability and selectivity with additional open stubs
Coupling matrix extracted TEM resonator networks [39]	Matrix-driven synthesis; extract Z_{oe}, Z_{oo} for parallel/end-coupled resonators; selectivity set by M_{ij} and external couplings	High	Slot size/period	Coupling matrix M
Multi-CL & short stub-SIR [40]	Extra stubs/SIRs shape passbands	High	Stub/SIR parameters	Quad-band
UTL & three λ/4 shunt stubs; add short-circuited T-shaped λ/4 resonator [45]	SWB passband from stub-loaded UTL; T-shaped resonator injects two controllable notch zeros; coupling controlled by inter-resonator gap	Medium	Stub lengths L6 (1st notch) & L5 (2nd notch); gap G (sets coupling k)	SWB 2.5–16.8 GHz (5 poles)
Edge-coupled BPF & movable SRR pair [46]	5th-order edge-coupled Chebyshev BPF; SRR pair is tuned to resonate in the stopband and the passband	Medium-High	Coupling w/s (filter); SRR displacement dx, SRR size (sensor)	two-substrate stack (SRRs above feed)
Parallel-connected open-loop microstrip resonators [52]	Chained low-order polynomials place RL zeros and shape S_{11}, S_{21}; narrowband passband with reduced sensitivity vs. Chebyshev	Medium	Seed set { 2,2} & coupling K via gap S.	Sub-6 GHz C-band design method; synthesis from Y_e/Y_o
Dual-band ABPF: CL & square SRR with two absorptive branches [53]	SRR-embedded CL creates two passbands; complementary band stop absorptive branches realize full-band absorption; RSLS provide high-impedance harmonic rejection	Medium-High	Impedance ratio IR (TZ spacing), R1/R2 (absorption), RSLS dims	two-port all-frequency reflectionless; suppression up to 10f0
Three CL lines with open/short stubs [54]	TZs near the passband from coupled lines; stepped-impedance I/O creates multiple attenuation poles	Medium	s, θ_3 θ_4 (TZs), l2	Tunable response with added stubs
Three pairs of coupled lines and SI stubs [55]	Multiple TPs/TZs from TPCL; stubs add edge TZs and sharper roll-off	Medium-High	k1 (FBW), Z_1, Z_2 (edge-TZs/roll-off), k2 (stopband)	Tunable response with added stubs
Quasi-reflectionless filters using CLs (BPF) & T-shaped BSF [57]	Duplexer-style combination with matched 3 dB FBWs; lossy path absorbs reflections	Medium	CL k (sets BPF FBW) & T-stub ratio m=Z_2/Z_1 (sets BSF FBW)	Single- and two-port QR BPF/BSF
Filtering switch via direct synthesis with PIN-loaded resonators [58]	Direct synthesis of an Nth-order BPF with N ON-state TZs; ideal transformers used to set element values; OFF-state TZs positioned to realize isolation	Medium-High	Order N and TZ placement (ON/OFF)	Two prototypes (30% and 50% FBW)

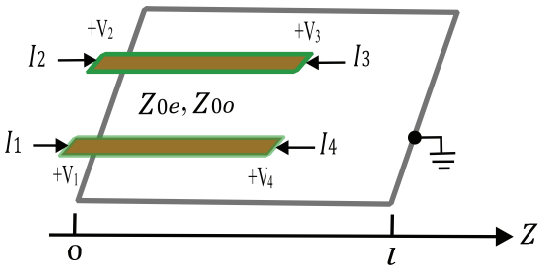

FIGURE 2. Schematic of a DCL filter with even- and odd-mode excitation.

into symmetric and antisymmetric modes, each having a distinct characteristic impedances [52]. A CL section can be modeled as a four-port network, where each port represents a location of voltage and current interaction as illustrated in Fig. 2. Among the various configurations possible in a four-port CL system, two are of particular interest in this study: all-pass filter and BPF configurations. In the all-pass filter configuration shown in Fig. 3(a), the input and output ports are positioned such that CLs function as a single transmission line. This setup does not significantly alter the amplitude of passing signal across frequencies, allowing nearly all frequencies to pass through uniformly. However, it introduces phase shifts, a defining trait of all-pass behavior. In contrast, the BPF configuration shown in Fig. 3(b) places the output port on the second line, resulting in mode conversion between even- and odd-modes. This interaction creates constructive and destructive interference effects, producing a frequency-selective response that enables BP characteristics. All currents and voltages are labeled at each port. The circuit has been analyzed using both even- and odd-mode techniques. Two ports need to be opened to change this network from a 4-port to a 2-port setup for filter operation. Two of the ten potential canonical filters [2] are chosen for this study, as illustrated in Fig. 3.

The image impedance is a vital analytical tool for understanding the behavior of microwave filters. It defines the input impedance of a network when the output is terminated with the same impedance and helps predict whether a structure will behave as an LP, HP, BP SB, all-stop, or all-pass filters. There are two reasons for concentrating on these two types: Fig. 3(a) illustrates the effect of neighboring lines on the transmission line filter, while Fig. 3(b) compares this topology to the proposed filter. The image input impedance of Fig. 3(a) is provided by [66]

$$Z_{i1} = \frac{Z_{0e} + Z_{0o}}{2} \tag{4}$$

where Z_{0e} and Z_{0o} are the even- and odd-impedance, respectively. In this case, the line is considered an all-pass filter. This means that the CL is still operated as a single line. To solve this, the output port is placed on the second line as illustrated in Fig. 3(b). Now, the image input impedance is given by [66]

$$Z_i = \frac{\sqrt{(Z_{0e} - Z_{0o})^2 - (Z_{0e} + Z_{0o})^2 \cos^2\theta}}{2\sin\theta} \tag{5}$$

Equation (5) indicates that the line operates as a BPF. Multiple cascaded sections are connected to achieve specific filter performance and a smoother BPF response [20, 40, 62]. This paper concentrates on a single section to minimize extra PCB area, without emphasizing the details of cascading sections.

2.2. Tri-Coupled Line Filter

In this subsection, the analysis shifts DCLs configuration to a more advanced topology involving three parallel coupled microstrip lines, also known as a tri-coupled line (TCL) filter. This configuration aims to explore the effect of inter-line coupling on the filter's frequency response and investigate the possibility of achieving enhanced BP behavior through structural modification. The structure under investigation consists of three microstrip lines, denoted as line a (bottom), line b (middle), and line c (top), which are illustrated in Fig. 4. Each line is terminated with an input and an output port, resulting in a six-port network. For analytical tractability, it is assumed that:

- Coupling occurs only between adjacent lines: i.e., between line a and line b, and between line b and line c
- Lines a and c are electrically isolated, indicating that no direct electromagnetic coupling is considered between them.

This approximation simplifies the analysis while preserving the essential physics of adjacent line coupling. Similar to manipulating a 4-port network, the $[Z]$ or impedance matrix, which contains 36 elements, can be derived for the proposed 6-port network. To convert the six-port network into a 2-port filter, all ports are open-circuited except ports 2 and 5, resulting in

$$Z_{22} = Z_{55} = \frac{-j}{2}(Z_{0e} + Z_{0o})\cot\theta \tag{6a}$$

$$Z_{25} = Z_{52} = \frac{-j}{2}(Z_{0e} + Z_{0o})\csc\theta \tag{6b}$$

The input image impedance of the filter can be calculated in the same manner as mentioned in [66] but the case of the six-port as

$$\begin{aligned} Z_i &= \sqrt{Z_{22}^2 - \frac{Z_{22}Z_{25}^2}{Z_{55}}} \\ &= \frac{1}{2}\sqrt{(Z_{0e} + Z_{0o})^2 \csc^2\theta - (Z_{0e} + Z_{0o})^2 \cot^2\theta} \\ &= \frac{Z_{0e} + Z_{0o}}{2} \end{aligned} \tag{7}$$

Equation (7) shows that the TCL configuration remains an all-pass filter and is the same as Equation (4). To turn it into a BPF, a change must be made to the midline, as explained in the next subsection.

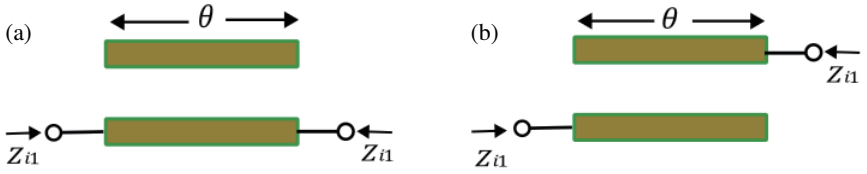

FIGURE 3. (a) DCL all-pass filter. (b) DCL BPF.

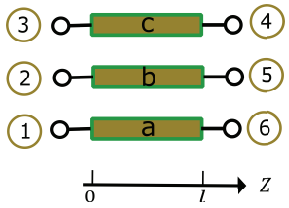

FIGURE 4. Geometry of the TCL configuration.

2.3. Tri-Coupled Line BPF

This subsection introduces a significant structural modification: a physical gap or split at the center of the midline (line b), illustrated in Fig. 5, following the demonstration that a symmetric TCL structure functions as an all-pass filter. The resulting filter is called TCL BPF. The physical gap serves two essential functions:

- Break the symmetry of the transmission path, disrupting uniform signal propagation and allowing for frequency discrimination.
- Introduce a capacitive discontinuity, which can be mathematically modeled as a pair of coupling capacitors. The coupling capacitors facilitate resonant behavior, a crucial feature for achieving BP filtering.

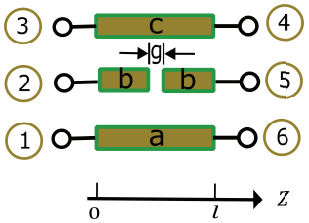

FIGURE 5. The proposed TCL BPF filter.

As illustrated in Fig. 5, line b is split into two equal-length $(l_b - g)/2)$ segments, separated by a small gap of width g. This results in:

- Two physical discontinuities within line b
- The creation of a coupling capacitive C_c between the two disconnected segments.

Significantly, while the outer lines (a and c) remain unaltered, they still contribute coupling to each half of the segmented center line. This preserves the adjacent-line interaction while allowing the inserted gap to become the dominant factor shaping the response. The analysis of even- and odd-modes can be performed as illustrated in Fig. 6. For simplicity, the gap width is assumed to be very small to get the length of the modeled midline segment to be approximately equal to $l_b/2$ instead of $(l_b - g)/2)$.

To analyze the electromagnetic behavior of this modified structure, even- and odd-mode decomposition is employed as depicted in Fig. 6:

- Even-mode excitation refers to simultaneous, in-phase currents at symmetric ports.

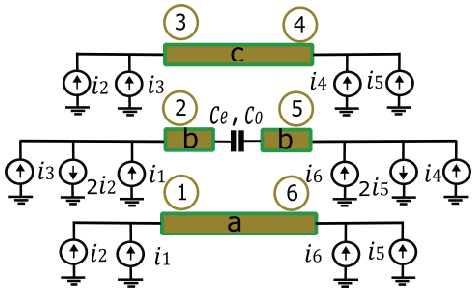

FIGURE 6. Analysis of TCL BPF in even- and odd-modes.

- Odd-mode excitation involves anti-phase signals.

The gap introduces different effective capacitances for both modes due to the altered current distribution and interaction with the electromagnetic field. The even- and odd-coupling capacitances are c_e and c_o, respectively. The Z-parameters for this 2-port filter (ports 2 and 5) can now be expressed in terms of these modal capacitances. Using transmission line theory and boundary conditions at the gap, the derived Z-elements incorporate transmission and coupling terms, thereby determining the filter response.

The total port currents, I_i, can be represented by the even- and odd-mode currents as

$$\begin{aligned} &I_1 = i_1 + i_2, \quad I_2 = i_1 - 2i_2 + i_3, \quad I_3 = i_2 + i_3, \\ &I_4 = i_4 + i_5, \quad I_5 = i_4 - 2i_5 + i_6, \quad I_6 = i_5 + i_6 \end{aligned} \tag{8}$$

where i_1, i_3, i_4, and i_6 are the driven even-mode currents, and i_2 and i_5 are the odd-mode driven currents. The voltages at ports 2 and 5 of line b, due to even-mode currents $(i_1,\ i_3,\ i_4,\ i_6)$ and odd-mode currents $(-2i_2,\ -2i_5)$, can be determined using circuit and transmission line theory. The Z-elements of a two-port network filter are derived to be

$$\begin{aligned} Z_{22} = Z_{55} \ = \ & \frac{1}{2}\left[Z_{0e} \frac{Z_{Le} + jZ_{0e}\tan\frac{\theta}{2}}{Z_{0e} + jZ_{Le}\tan\frac{\theta}{2}} \right. \\ & \left. + Z_{0o} \frac{Z_{Lo} + jZ_{0o}\tan\frac{\theta}{2}}{Z_{0o} + jZ_{Lo}\tan\frac{\theta}{2}} \right] \end{aligned} \tag{9a}$$

$$\begin{aligned} Z_{25} = Z_{52} \ = \ & -j\left[\frac{Z_{0e}^2}{Z_{0e}\sin\theta + j2Z_{Le}\sin^2\frac{\theta}{2}} \right. \\ & \left. + Z_{0e} \frac{Z_{0o}^2}{Z_{0o}\sin\theta + j2Z_{Lo}\sin^2\frac{\theta}{2}} \right] \end{aligned} \tag{9b}$$

where

$$Z_{Le} = -j\left(\frac{1}{\omega c_e} + Z_{0e}\cot\frac{\theta}{2}\right) \quad (10a)$$

$$Z_{Lo} = -j\left(\frac{1}{\omega c_o} + Z_{0o}\cot\frac{\theta}{2}\right) \quad (10b)$$

The first terms inside the parentheses of Equations (10a) and (10b) represent the capacitive reactance contributions of even- and odd-mode coupling, specifically $\frac{1}{\omega c_e}$, $\frac{1}{\omega c_o}$, respectively. As the physical gap width g becomes very small approaching zero, the corresponding coupling capacitances c_e and c_o increase dramatically, theoretically tending toward infinity based on standard capacitance relations. This causes the reactance terms $\frac{1}{\omega c_e}$ and $\frac{1}{\omega c_o}$ in Equations (10a) and (10b) to approach zero, effectively nullifying their influence on the network parameters. Consequently, Equations (9a) and (9b) are simplified to the earlier forms given in Equations (6a) and (6b), respectively. Under this limiting case, the input impedance Z_i is simplified to the form given in Equation (7), which corresponds to that of an all-pass filter. Under this condition, the two previously separated sections of line b are effectively reconnected, becoming electrically continuous. This design technique enables dynamic control of the signal path and frequency response by adjusting the central gap, allowing for precise tuning of the filter's performance.

2.4. Effect of Even- and Odd-Capacitance of the TCL Filter Response

This subsection examines how the even-mode and odd-mode capacitances affect the electrical behavior of the TCL filters, particularly the image impedance Z_i, and ultimately determines whether the structure functions as an all-pass filter or a BPF. The even- and odd-mode capacitances critically determine the filter response, as evident in Equations (7), (9), and (10). To analyze this effect, let's consider the governing equations for these quantities.

$$c_e = \frac{c_{gg} + c_{gb}}{2} \quad (11a)$$

$$c_o = \frac{c_{gg} - c_{gb}}{2} \quad (11b)$$

Here, c_{gg} denotes the self-capacitance between the two separated segments of the central line (line b), introduced by the physical gap. At the same time, c_{gb} represents the mutual capacitance between the midline and adjacent outer lines (lines a or c). These two capacitances, c_{gg} and c_{gb}, determine the strengths of the even and odd modes, which significantly influence the filter's modal behavior. When the physical gap width becomes very small, the self-capacitance c_{gg} increases substantially due to strong electric field coupling across the thin dielectric or air gap separating the central line segments. Conversely, when the three lines are positioned very close together, the mutual capacitance c_{gb} also increases, driven by the strong coupling between the midline and outer lines. These variations in c_{gg} and c_{gb} directly affect the loaded reactances Z_{Le} and Z_{Lo}, as exposed in Equations (10a) and (10b), where Z_{Le} and Z_{Lo} are used to compute the elements of Equation (9) and are then substituted into Equation (10). As a result, the coupling capacitance setup ultimately determines the overall filter response. The real part of the image impedance, $Re(Z_i)$, is a key indicator of how the filter will behave across frequencies. When $Re(Z_i)$ is non-zero and frequency-dependent, it indicates energy transmission at specific frequencies, confirming BPF behavior. Conversely, if $Re(Z_i)$ remains zero, the structure acts as an all-pass filter or a non-transmitting medium. Fig. 7 compares $Re(Z_i)$ versus the electrical length θ in three cases: $c_{aa} > c_{ab}$, $c_{aa} = c_{ab}$, and $c_{aa} < c_{ab}$.

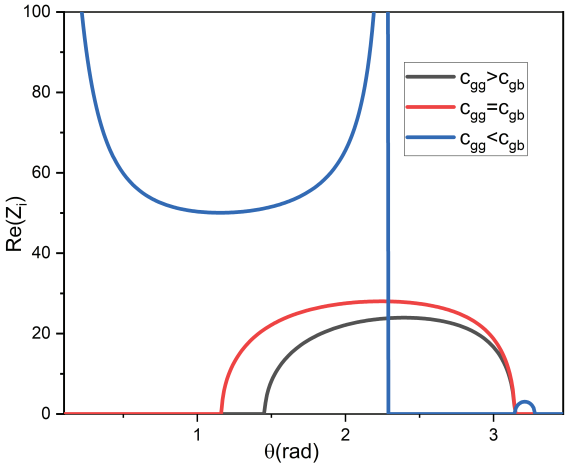

FIGURE 7. Effect of capacitance configuration on $Re(Z_i)$ versus electrical length θ for the TCL filter. The case $c_{gg} = c_{gb}$ yields a broader passband (wider θ span with non-zero $Re(Z_i)$), whereas $c_{gg} > c_{gb}$ produces a narrower passband with sharper peaks; $c_{gg} < c_{gb}$ does not sustain a robust bandpass.

As mentioned earlier, $Re(Z_i)$ values serve as the primary indicator of filter response. These values, depicted in Fig. 7, demonstrate that when $c_{gg} > c_{gb}$ and $c_{gg} = c_{gb}$, the BP response is achieved. Although the presence of g does not appear in the derived equations, its effect has been accounted for c_e and c_o. Moreover, the effect of g on c_{gg} and c_{gb}, which modifies the filter response, is explained in the next section. The two cases of $c_{gg} > c_{gb}$ and $c_{gg} = c_{gb}$ indicate no transition from BPF to SBF or another topology. The emphasis will be on ensuring that c_{gg} is greater than or equal to c_{gb}. The bandwidth of the passband depends on the relative magnitudes of $c_{gg} and c_{gb}$. When $c_{gg} = c_{gb}$, $Re(Z_i)$ remains non-zero over a wider θ interval, corresponding to a broader passband. When $c_{gg} > c_{gb}$, $Re(Z_i)$ peaks become sharper and more confined in θ, indicating a narrower passband. This trend follows from the loading terms in Equations (10a) and (10b): larger c_{gg} increases the capacitive loading across the midline gap and tightens the passband, whereas balancing the self and mutual capacitances ($c_{gg} = c_{gb}$) relaxes this loading and broadens the passband. Configurations with $c_{gg} < c_{gb}$ are avoided in practice due to degraded bandpass behavior (weak/insufficient $Re(Z_i)$).

3. RESULTS AND DISCUSSION

3.1. Geometric Synthesis of Line Width and Physical Length in TCL BPF

To determine the conductor width W and convert electrical lengths into physical copper lengths, a target characteristic impedance Z_0 is specified for each line. Closed-form microstrip equations are then used to find the effective permittivity ε_{eff} and width ratio W/h. With ε_{eff} evaluated at the design frequency f_0, the guided wavelength λ_g follows to estimate the physical copper lengths. The (lossless, $t \approx 0$) effective permittivity of a microstrip line on a substrate with relative permittivity ε_r and height h is given by [66]

$$\varepsilon_{eff} = \frac{\varepsilon_r + 1}{2} + \frac{\varepsilon_r - 1}{2} \frac{1}{\sqrt{1 + 12h/W}} \tag{12}$$

given ε_{eff}, the characteristic impedance Z_0 is [66]

$$Z_0 = \begin{cases} \frac{60}{\sqrt{\varepsilon_{eff}}} \ln\left(\frac{8h}{W} + \frac{W}{4h}\right), & W/h \leq 1 \\ \frac{120\pi}{\sqrt{\varepsilon_{eff}}(W/h + 1.393 + 0.667 \ln(W/h + 1.444))}, & W/h \geq 1 \end{cases} \tag{13}$$

For design purposes, the inverse relations W/h are useful as

$$\frac{W}{h} = \begin{cases} \frac{8e^A}{e^{2A} - 2}, & W/h < 2 \\ \frac{2}{\pi}\left[B - 1 - \ln(2B - 1) + \frac{\varepsilon_r - 1}{2\varepsilon_r}\left(\ln(B - 1) + 0.39 - \frac{0.61}{\varepsilon_r}\right)\right], & W/h > 2 \end{cases} \tag{14}$$

where

$$A = \frac{Z_0}{60}\sqrt{\frac{\varepsilon_r + 1}{2}} + \frac{\varepsilon_r - 1}{\varepsilon_r + 1}\left(0.23 + \frac{0.11}{\varepsilon_r}\right) \text{ and}$$

$$B = \frac{377\pi}{2Z_0\sqrt{\varepsilon_r}}$$

For each line in TCL BPF, a target Z_0 is selected, and W is determined using Equation (14); then ε_{eff} is updated with Equation (12). The guided wavelength at the center frequency f_0 of each line is

$$\lambda_g = \frac{c}{f_0\sqrt{\varepsilon_{eff}}} \tag{15}$$

In the current TCL BPF, each line is designed as a half-wavelength at f_0. Therefore, the electrical length l_e is

$$l_e = \frac{\lambda_g}{2} \tag{16}$$

where the midline is divided by a small central gap, which is much smaller than the line length itself and can be excluded from current calculations. To convert electrical lengths to physical copper lengths, the open-end fringing correction ΔL (per open end) is applied as [69]

$$\frac{\Delta L}{h} \approx 0.412 \frac{(\varepsilon_{eff} + 0.3)(W/h + 0.264)}{(\varepsilon_{eff} - 0.258)(W/h + 0.8)} \tag{17}$$

The three lines have six open edges; therefore, the physical length of the fabricated lines is

$$l_p \approx l_e - 6\Delta L \tag{18}$$

Let's analyze a numerical example to determine the width and length of the three lines that constitute the TCL BPF filter operating at 2.4 GHz. These dimensions are also pertinent for the simulated TCL filter in the subsequent subsection. The three lines are printed on an FR4 PCB with $\varepsilon_r = 4.3$ $h = 1.445$ mm and $Z_0 = 50\,\Omega$ applicable to all. Equations (14) and (15) give $W = 2.81$ mm and $\lambda_g = 68.50$ mm; consequently, $l_e = 34.25$ mm. Utilizing Equation (17) with $\varepsilon_{eff} = 3.33$ yields $\Delta L = 0.566$ mm for each open end, so the physical length of each line will be $l_p = 30.85$ mm.

3.2. Simulation of TCL BPF

3.2.1. Gap and Space Configuration

The filter proposed in Fig. 5 can be simulated using Computer Simulation Technology (CST) Microwave Studio (CST MWS). The properties of the FR4 PCB on which the filter is constructed are selected to be consistent with those parameters outlined in the preceding subsection. The substrate dimensions are $50 \times 50\,\text{mm}^2$, and the strip thickness $t = 0.035$ mm. The spacing between adjacent lines is $s = 1$ mm, and the central gap is $g = 0.5$ mm. The transmission coefficient (S_{21} or S_{12}) is the primary parameter determining the filter response. To compare this filter with the DCL filter in Fig. 3(b), the same parameters such as length width and spacing have been used. The transmission coefficients of the two filters are displayed in Fig. 8.

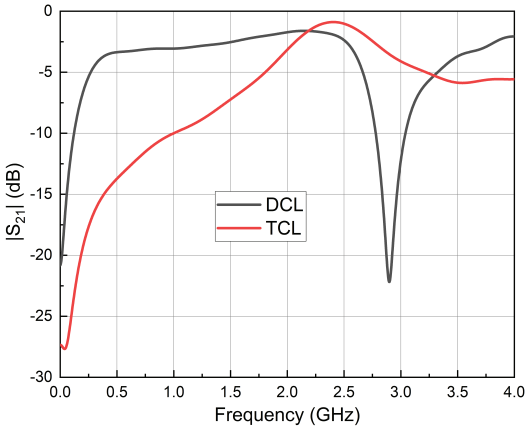

FIGURE 8. Transmission coefficient of the DCL and TCL BPFs.

At the target center frequency of 2.4 GHz, both filters are subjected to comparative analysis. As depicted in Fig. 8, the TCL filter exhibits a narrower bandwidth than the DCL counterpart. Furthermore, the transmission coefficient at the center frequency is notably enhanced, rising from -6.87 dB for the DCL filter to -0.89 dB for the TCL filter. Fig. 9 shows how g influences the performance of the TCL filter, indicating that as g increases, the TCL filter becomes more selective, mak-

TABLE 2. Effect of substrate (M1–M7) on TCL BPF dimensions and area at 2.4 GHz.

Label	Material	ε_r	tan δ	W (mm)	l_p (mm)	l_{pn} (mm)	area (mm^2)
M1	Rogers RT5880 LZ	2.0	0.0021	4.770	44.45	44.45	724.98
M2	Rogers RO4003C	3.5	0.0027	3.370	34.45	34.45	417.19
M3	FR-4	4.3	0.0250	2.810	30.85	31.25	325.94
M4	Rogers RO4360G2	6.4	0.0038	2.062	26.12	26.2	214.47
M5	Alumina	9.9	0.0001	1.384	21.5	21.5	132.27
M6	Rogers RO3010	11.2	0.0021	1.223	20.34	20.17	114.33
M7	Rogers TMM 13i	12.2	0.0019	1.118	19.58	19.33	103.49

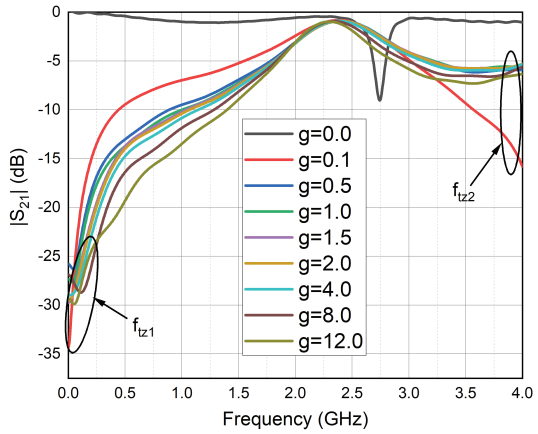

FIGURE 9. Transmission coefficient of the TCL BPF for different values of g.

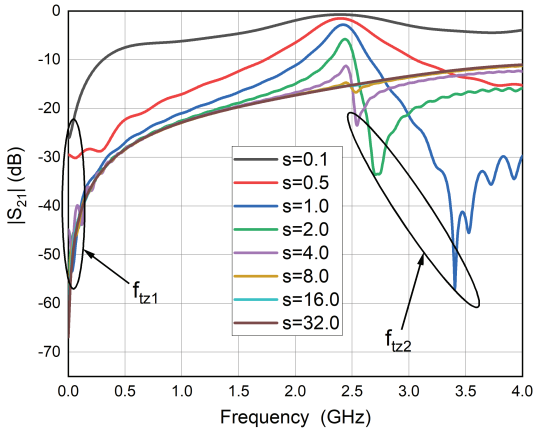

FIGURE 10. Transmission coefficient of the TCL BPF for different values of s.

ing it highly versatile for various microwave applications. As the parameter g increases from 0.5 mm to 12 mm, a series of capacitive discontinuities develop between the separated midlines. Furthermore, the effective area between the reduced midlines and coupled lines diminishes, resulting in a decrease in self-capacitance C_{gg} and mutual capacitance C_{gb}. This also causes a decline in the values of C_e and C_o, as explained in Equations (11a) and (11b). These changes result in an increase in the modal reactances $\frac{1}{\omega c_e}$ and $\frac{1}{\omega c_o}$, as illustrated in Equations (10a) and (10b). Therefore, the real part of the impedance in Equation (7), $Re(Z_i)$, drops within the stopband, thereby improving the suppression level in the $|S_{21}|$ stopband region. The passband frequency, particularly in the vicinity of the central frequency, appears to remain unaffected because, at the resonance frequency, all reactances are nullified. The other parameter to examine is the spacing (s). From a circuit perspective, increasing s decreases the mutual capacitance C_{gb}, which, according to Equations (11a) and (11b), also reduces modal capacitances C_e and C_o. This leads to an increase in modal reactances $\frac{1}{\omega c_e}$ and $\frac{1}{\omega c_o}$ (referencing Equations (10a) and (10b)), thus limiting energy transfer across the structure and affecting $Re(Z_i)$. These changes influence the transmission properties, as shown in Fig. 10. In this scenario, the response approaches a weakly coupled or nearly all-stop behavior, causing the bandpass to effectively collapse. For FR-4 implementations, a practical range of $0.5\,\text{mm} \leq s \leq 2.0\,\text{mm}$ offers an ideal compromise — ensuring strong coupling — while keeping manufacturability in check compared to the very small values of s. Currently, two cases are selected: the first involves adjusting the gap width, and the second pertains to the spacing between elements. Based on initial observations of Figs. 9 and 10, and to enhance selectivity, the following values for g and s are set at 0.5 mm and 1 mm, respectively. The TCL BPF is then re-executed with these updated parameters. The resonance frequency slightly shifts to 2.43 GHz. As a result, the length is adjusted to 31.25 mm instead of 30.85 mm to reach the desired resonance frequency (2.4 GHz).

3.2.2. Substrate Effect

To perform a comprehensive parametric analysis of the TCL BPF, it is essential to examine the substrate material. This can be achieved by re-simulating the TCL BPF with different material types, each distinguished by specific ε_r and Loss tangent (tan δ). Emphasizing permittivity is crucial as it forms the foundation of the design. Since it appears in all design equations related to the microstrip line and considering that the filter mainly depends on geometrical parameters, both the width and length are constrained by it. Seven substrate materials (M1–M7) are listed in Table 2, ranging from lower permittivity M1

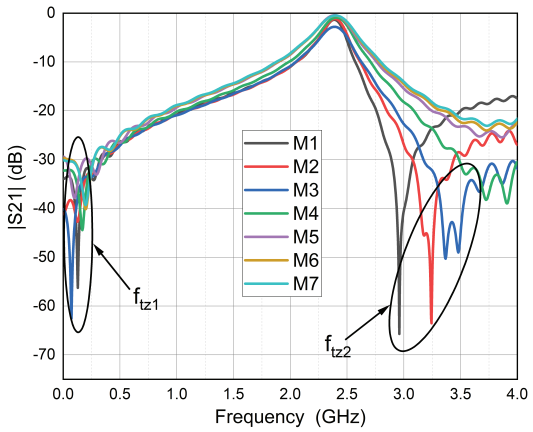

FIGURE 11. Transmission coefficient of the TCL BPF for different material types.

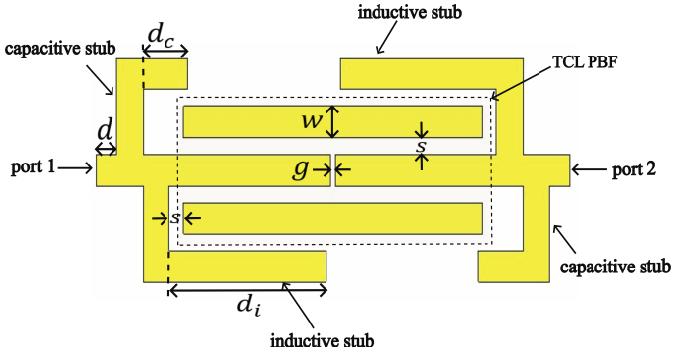

FIGURE 12. Layout of the proposed TCL BPF showing the locations of the auxiliary stubs (all sections having the same width).

to higher permittivity M7, including FR-4 as previously explained. These materials are downloaded from the material library in the CST MWS environment. Initially, the physical length and width are recalculated using the design equations outlined in Subsection 3.1. With a fixed coupling geometry ($g = 0.5$ and $s = 1.0$), rescaling the physical length is necessary to achieve the desired center frequency of 2.4 GHz. Variations in g and s cause minor shifts in the resonance frequency, as observed earlier. To tune the center frequency to 2.4 GHz, an updated physical length (l_{pn}) is used, employing a slight sweep to reach the target frequency. As illustrated in Fig. 11, the most effective suppression level occurs when using a low permittivity material M1. This is due to parasitic capacitances between each element of the TCL BPF and the ground, which increase with higher dielectric constants and subsequently decrease $Re(Z_i)$, affecting the transmission coefficient $|S_{21}|$. Therefore, this filter is suitable for low-cost PCBs with low permittivity, such as FR-4. Conversely, when miniaturization is critical, a high-permittivity substrate is preferred. Relative to M1, using M7 reduces the estimated footprint by 85.73% with respect to material M1, which is a significant achievement. The areas in Table 2 are computed as: $area = l_{pn}(3W + 2s)$ (with $s = 1$ mm). At this point, there are two TZs occurring at the left and right sides of the center frequency. These frequencies are stated in Figs. 9, 10, and 11. The subsequent subsection elucidates the augmentation of TZs through the incorporation of open stubs into the proposed filter, which results in a more precise bandwidth and ensures that the filter aligns with 50.

3.2.3. Tuning of TCL BPF

The proposed TCL BPF features two complementary tuning approaches: (i) geometric coupling, which involves the central gap g in the midline and the inter-line spacing s, primarily influencing the passband fractional bandwidth (FBW) and the band-edge roll-off through the modal capacitances C_{gg} and C_{gb} and (ii) auxiliary resonant loading using a pair of shunt open stubs, one capacitive and one inductive, which accurately position TZs and improve in-band matching. Together, these components form a compact single-section filter characterized by controllable selectivity and adaptable transition-band behavior. A short open stub ($Lc < \lambda g$), which exhibits capacitive characteristics near f_0, is used to enhance the roll-off at the lower band edge and improve rejection on the low side. Conversely, a long open stub ($Li > \lambda g$), functioning inductively, is employed to reinforce the roll-off at the upper band edge and improve rejection on the high side. Each open stub resonates when its electrical length approaches ($\lambda g/4$), at which point it acts as a shunt short and creates a TZ. For a shunt open stub with characteristic impedance Z_s and electrical length θ, the normalized susceptance is given by

$$b_{stub}(\omega) = \frac{B_{stub}}{Y_0} = \frac{Z_0}{Z_s}\tan(\theta), \quad \theta = \beta l \tag{19}$$

Here $b_{stub}>$ (capacitive behavior) for $< \theta < \pi$ and $b_{stub}<$ (inductive behavior) for $\pi/2 < \theta < \pi$. By selectively combining these stubs, additional TZs are generated near the band edges, thereby enhancing selectivity. Fig. 12 illustrates the positions of these stubs, which possess short capacitive and long inductive lengths ($Lc < \lambda g/4$) and ($Li > \lambda g/4$), respectively. These stubs are bent and routed along the coupled lines to maintain a compact footprint and enhance coupling. The lengths of the two stubs are determined by the entire path, expressed as: $Lc = dc + 2s + 2w$ and $Li = di + 2s + 2w$. The distance s between the inductive stub and coupled line is established to prevent contact. The capacitive stub is connected directly to the inductive stub with zero distance, but not in the same position, to prevent it from being perceived as a single stub. The two stubs are placed on either side of the proposed filter in a reversed arrangement. Each port is connected to the tuned TCL BPF via a feeding section dd for preparing the SMA connector. This structure is designed on FR-4 material and optimized in CST MWS to produce the following compact set (all in mm): $W = 2.81$ (for all sections), $l = 28.9$, $s = 1.37$, $g = 0.5$, $Lc = 12.1$, $Li = 24.5$, and $d = 1$. Fig. 13 shows snapshots of the magnitude of surface current density $|J|$, which repeats every π. Specifically, pairs of snapshots separated by π have the same $|J|$ magnitudes, with only a sign change in the phasor representation. Therefore, subfigures (a) and (e) correspond to the same excitation phases at $\theta = 0$ and π, respectively, as well as (b) and (f) at $\pi/4$ and $5\pi/4$, and similarly for {(c), (g)} and {(d),

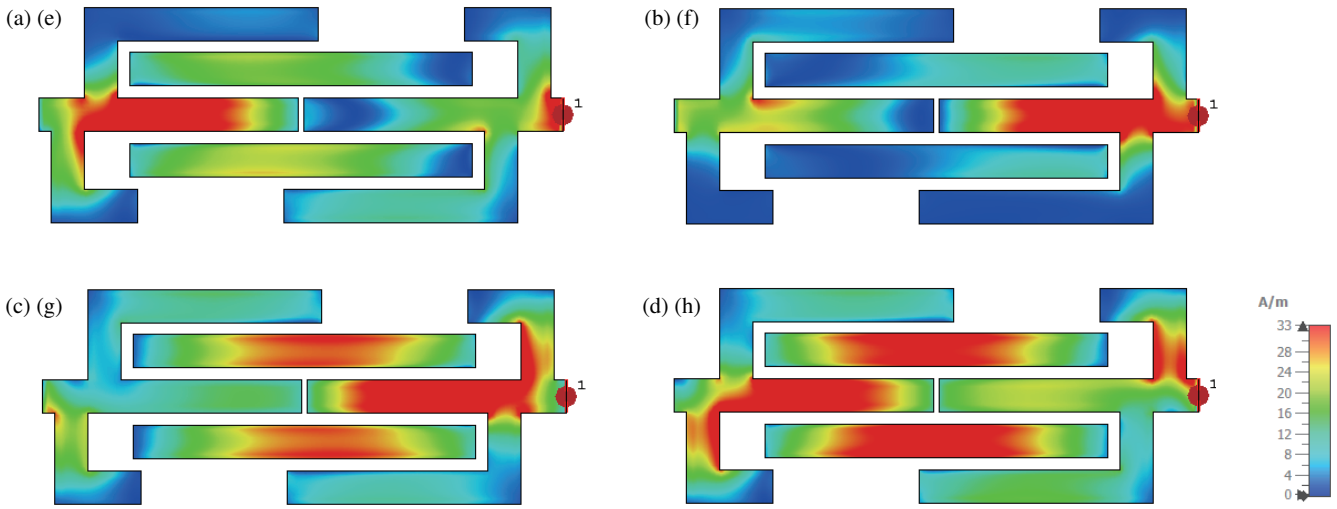

FIGURE 13. Magnitude of the surface current density of the TCL BPF at various phase angles: (a) 0, (b) $\pi/4$, (c) $\pi/2$, (d) $3\pi/4$, (e) π, (f) $5\pi/4$, (g) $3\pi/2$, and (h) $7\pi/4$. (The snapshots are taken from the back view of Fig. 12).

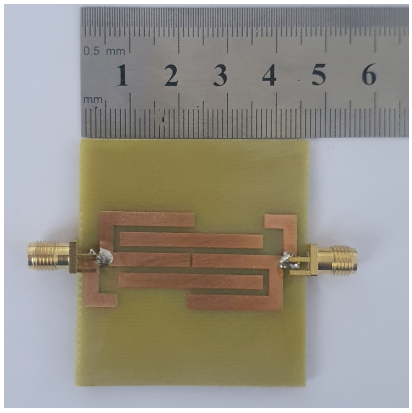

FIGURE 14. Implementation of proposed TCL BPF.

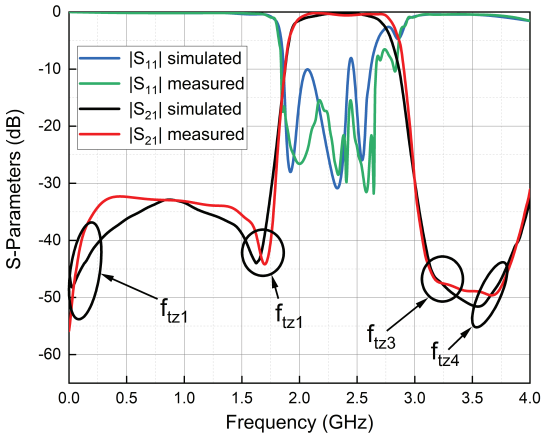

FIGURE 15. Simulated and measured transmission coefficients of the TCL BPF.

(h)}. Due to the mirror symmetry inherent in the layout and the central capacitive gap, these subfigures can also appear visually similar across non-π-separated pairs, such as (f) and (a). When analyzing the dominant hot-spots near the gap and outer rails, it is essential to recognize that strict periodic pairings occur between points separated by π. The recurring hot-spots at the gap edges confirm that the inserted capacitive discontinuity governs the resonance behavior. Additionally, phase-shifted peaks observed on the open stubs indicate how auxiliary stubs facilitate the injection of near-edge TZs, thereby enhancing the overall response. The transmission and reflection characteristics, or S-parameter responses, of the simulated TCL BPF are shown in Fig. 15. The transmission zeros at f_{tz1} and f_{tz4} are inherent to the TCL BPF itself, while f_{tz2} and f_{tz3} result from the capacitive and inductive stubs, respectively. At the center frequency of 2.4 GHz, the insertion loss is 0.54 dB. The lower and upper cutoff frequencies at the 3 dB and 20 dB points are identified as: $f^l_{3dB} = 1.93$ GHz, $f^l_{20dB} = 1.82$ GHz, $f^u_{3dB} = 2.80$ GHz, and $f^u_{20dB} = 2.95$ GHz. These frequencies correspond to bandwidths of 0.87 GHz and 1.13 GHz at the 3 dB and 20 dB levels, respectively. Therefore, the shape factor (SF) can be determined as $SF = BW_{20dB}/BW_{3dB}$ [70] and equals 1.3.

3.3. Measurement Results and Comparative Analysis

The simulated and practical results substantially reinforce the theoretical foundations and modeling methodologies discussed previously. By incorporating a central gap along the midline of a TCL filter, a distinct transition from an all-pass to a narrow bandpass response is realized. Key performance indicators, including center frequency, transmission coefficient, and bandwidth characteristics, corroborate this transition both qualitatively and quantitatively. Physical prototypes, similar to those presented in Fig. 14, were fabricated to substantiate the simulation outcomes. The constructed TCL BPF demonstrates practical implementation on an FR4 substrate with a relative permittivity of 4.3. The experimental data align closely with the simulated predictions, thereby confirming that a cen-

TABLE 3. Comparative performance analysis of the TCL BPF against representative state-of-the-art microstrip BPFs.

Ref	f_0 (GHz)	$\text{FBW}_{3\text{dB}}$ (%)	IL (dB)	$\text{SF}_{20\text{dB}}$	Circuit size ($\lambda g \times \lambda g$)
[34]	2.236*	22.4*	0.40*	2.0*	0.65 × 0.38
[37]	2.0	11	2.0	1.45*	0.49 × 0.30
[40]	6.15	8.1	0.4	2.0*	0.19 × 0.15*
[46]	2.0	10	2.80	1.59*	1.60 × 0.24
[50]	1.51	62.9	1.01	1.11	0.18 × 0.52*
[51]	3.0	60	0.80	1.22*	0.67 × 0.17*
[52]	3.50	1.14	2.50	1.65*	0.85 × 0.53*
[53]	2.63	9.7	1.47	1.27	1.52 × 1.09
[54]	1.30	65	0.25	0.57	0.25 × 0.12 *
[55]	1.45	34.4	1.0	1.26*	0.76 × 0.54
[57]	2.035	55*	0.40	1.14*	0.27 × 0.26*
This work	2.40	37.3	0.58	1.30	0.72 × 0.30

* Estimated from published plots.

tral gap and the addition of stubs serve as effective and tunable techniques for transforming an all-pass TCL structure into a TCL BPF with predictable and controllable frequency attributes, as verified through both simulation and empirical measurement. The performance of the TCL bandpass filter is analyzed using its scattering parameters $|S_{21}|$ (transmission) and $|S_{11}|$ (reflection), with the P9370A 2-port VNA utilized for S-parameter measurements, as illustrated in Fig. 15. Using the measured $|S_{21}|$, $f^l_{3dB} = 1.94$ GHz, $f^l_{20dB} = 1.82$ GHz $f^u_{3dB} = 2.83$ GHz and $f^u_{20dB} = 2.96$ GHz resulting in a center frequency $f0 = 2.39$ GHz, and a 3 dB bandwidth $BW_{3dB} = 0.89$ GHz ($FBW_{3dB} = 37.3\%$). Across the designated passband, the prototype demonstrates a return loss exceeding 20 dB, with the optimal case at the center frequency typically surpassing 30 dB. The measured $|S_{11}|$ values closely correspond to the simulated results; minor discrepancies (approximately 1–3 dB) are attributable to the tolerances in connector launch and variations in FR-4 parameters. Out-of-band behavior confirms sharp selectivity enabled by the central capacitive discontinuity and stubs, resulting in an SF = 1.3, consistent with the simulated results. Two transmission zeros are observed at approximately 1.68–1.72 GHz and 3.08–3.15 GHz, with peak rejection between 48 and 52 dB, establishing steep roll-off on both sides of the passband. In the upper stopband, $|S_{21}| < -35$ dB is maintained over the range of 3.10–3.20 GHz. The return loss at the center frequency is 30 dB, indicating a good level of performance. In comparison with recent studies involving CL and stub-loaded configurations, the proposed TCL BPF demonstrates competitive roll-off performance while requiring fewer resonators and eliminating the need for absorptive branches or complex cross-couplings. To ensure a fair comparison, results should be normalized to λ_0 at each resonant frequency f_0 on each substrate, using the same SF definition. The measured figures of merit, alongside a normalized comparison with recent CL and stub-loaded BPFs, are summarized in Table 3, providing a comprehensive performance analysis of the TCL BPF relative to prior research.

4. CONCLUSION

A single-section TCL bandpass filter featuring a centrally gapped midline has undergone comprehensive analysis, synthesis, and experimental validation. Even- and odd-mode decompositions, derived from image-impedance interpretations, clarify the transition from the all-pass response characteristic of symmetric TCLs to a selective bandpass upon the introduction of a capacitive discontinuity. The resulting modal capacitances (C_{gg}, C_{gb}) offer intuitive control via gap width and interline spacing to adjust bandwidth and edge steepness, while two shunt open stubs effectively position near-edge TZs and improve in-band matching, without necessitating higher-order, cross-coupling, or absorptive branches. A compact FR-4 prototype operating at 2.4 GHz achieved an insertion loss of approximately 0.58 dB, fractional bandwidth at 3 dB about 37.3%, shape factor around 1.3, and deep stopband notches 50 dB near 1.7 GHz and 3.1 GHz, with $|S_{21}| \leq -35$ dB across the 3.10–3.20 GHz range, thereby confirming both the analytical and CST simulation predictions. Substrate scaling analyses indicate that materials with low relative permittivity favor suppression and selectivity on cost-effective substrates, whereas high relative permittivity materials enable significant area reduction with predictable retuning. Overall, the proposed topology achieves a balanced combination of compactness, tunability, and high selectivity utilizing only one TCL section and two stubs. Future research may extend this methodology by incorporating reconfigurable spacing through the addition of a switchable diode, thereby enabling dynamic regulation of the coupling strength between the tri-coupled lines. Such an approach would facilitate real-time adjustment of the passband frequency and bandwidth, rendering the filter adaptable to multi-standard wireless systems. Furthermore, the integration of PIN diodes or varactors within the central capacitive gap could permit on-demand switching between narrowband and wideband modes, or even enable reconfigurable dual-band responses, which are highly advantageous in Internet of Things (IoT) 5G/6G, or UWB radar front-end applications.

REFERENCES

[1] Allen, J. L., "Inhomogeneous coupled-line filters with large mode-velocity ratios," *IEEE Transactions on Microwave Theory and Techniques*, Vol. 22, No. 12, 1182–1186, Dec. 1974.

[2] Mongia, R., I. J. Bahl, and P. Bhartia, *RF and Microwave Coupled-Line Circuits*, Artech House, Inc., 1999.

[3] Amari, S., "Sensitivity analysis of coupled resonator filters," *IEEE Transactions on Circuits and Systems II: Analog and Digital Signal Processing*, Vol. 47, No. 10, 1017–1022, Oct. 2000.

[4] Kuo, J.-T., W.-H. Hsu, and W.-T. Huang, "Parallel coupled microstrip filters with suppression of harmonic response," *IEEE Microwave and Wireless Components Letters*, Vol. 12, No. 10, 383–385, Oct. 2002.

[5] Yang, N., Z. N. Chen, Y. Y. Wang, and M. Y. W. Chia, "Studies on crossover and broadside-coupled microstrip bandstop filters," *Microwave and Optical Technology Letters*, Vol. 38, No. 3, 228–231, Aug. 2003.

[6] Chin, K.-S. and J.-T. Kuo, "Insertion loss function synthesis of maximally flat parallel-coupled line bandpass filters," *IEEE Transactions on Microwave Theory and Techniques*, Vol. 53, No. 10, 3161–3168, Oct. 2005.

[7] Lee, H.-M. and C.-M. Tsai, "Improved coupled-microstrip filter design using effective even-mode and odd-mode characteristic impedances," *IEEE Transactions on Microwave Theory and Techniques*, Vol. 53, No. 9, 2812–2818, Sep. 2005.

[8] Sun, S. and L. Zhu, "Periodically nonuniform coupled microstrip-line filters with harmonic suppression using transmission zero reallocation," *IEEE Transactions on Microwave Theory and Techniques*, Vol. 53, No. 5, 1817–1822, May 2005.

[9] Phromloungsri, R., M. Chongcheawchamnan, and I. D. Robertson, "Inductively compensated parallel coupled microstrip lines and their applications," *IEEE Transactions on Microwave Theory and Techniques*, Vol. 54, No. 9, 3571–3582, Sep. 2006.

[10] Chen, C.-C., J.-T. Kuo, M. Jiang, and A. Chin, "Study of parallel coupled-line microstrip filter in broadband," *Microwave and Optical Technology Letters*, Vol. 48, No. 2, 373–375, Feb. 2006.

[11] Chin, K.-S., Y.-C. Chiou, and J.-T. Kuo, "New synthesis of parallel-coupled line bandpass filters with Chebyshev responses," *IEEE Transactions on Microwave Theory and Techniques*, Vol. 56, No. 7, 1516–1523, Jul. 2008.

[12] Sun, S., L. Zhu, and H.-H. Tan, "A compact wideband bandpass filter using transversal resonator and asymmetrical interdigital coupled lines," *IEEE Microwave and Wireless Components Letters*, Vol. 18, No. 3, 173–175, 2008.

[13] Mohra, A. S., "Coupled microstrip line bandpass filter with harmonic suppression using right-angle triangle grooves," *Microwave and Optical Technology Letters*, Vol. 51, No. 10, 2313–2318, Oct. 2009.

[14] Navarro-Cia, M., J. M. Carrasco, M. Beruete, and F. J. Falcone, "Ultra-wideband metamaterial filter based on electroinductive-wave coupling between microstrips," *Progress In Electromagnetics Research Letters*, Vol. 12, 141–150, 2009.

[15] Zhan, J.-S. and J.-L. Wang, "A simple four-order cross-coupled filter with three transmission zeros," *Progress In Electromagnetics Research C*, Vol. 8, 57–68, 2009.

[16] Fathelbab, W. M. and M. J. Almalkawi, "Narrowband filters with tightly coupled resonators," *IET Microwaves, Antennas & Propagation*, Vol. 4, No. 2, 269–276, Feb. 2010.

[17] Wu, H.-W., S.-K. Liu, M.-H. Weng, and C.-H. Hung, "Compact microstrip bandpass filter with multispurious suppression," *Progress In Electromagnetics Research*, Vol. 107, 21–30, 2010.

[18] Kang, I.-H., K. Wang, and S. M. Li, "Modified compact combline filter using planar parallel coupled structure with extended rejection bandwidth," *Journal of Navigation and Port Research*, Vol. 34, No. 7, 543–552, 2010.

[19] Packiaraj, D., K. J. Vinoy, M. Ramesh, and A. T. Kalghatgi, "Design of a compact wideband bandpass filter," *Microwave and Optical Technology Letters*, Vol. 52, No. 6, 1387–1389, Jun. 2010.

[20] Ye, C.-S., Y.-K. Su, M.-H. Weng, C.-Y. Hung, and R.-Y. Yang, "Design of the compact parallel-coupled lines wideband bandpass filters using image parameter method," *Progress In Electromagnetics Research*, Vol. 100, 153–173, 2010.

[21] Xiao, K., L. F. Ye, F. Zhao, S.-L. Chai, and J. L.-W. Li, "Coupling matrix decomposition in designs and applications of microwave filters," *Progress In Electromagnetics Research*, Vol. 117, 409–423, 2011.

[22] Ho, M.-H. and P.-F. Chen, "Suspended substrate stripline bandpass filters with source-load coupling structure using lumped and full-wave mixed approach," *Progress In Electromagnetics Research*, Vol. 122, 519–535, 2012.

[23] Omote, Y., T. Yasuzumi, T. Uwano, and O. Hashimoto, "Ultra-wideband bandpass filter using matching-lines and interdigital filter with close-coupled resonators," *IEICE Electronics Express*, Vol. 9, No. 7, 660–665, 2012.

[24] Xu, X. and W. Wu, "Compact microstrip dual-mode dual-band bandpass filters using stubs loaded coupled line," *Progress In Electromagnetics Research C*, Vol. 41, 137–150, 2013.

[25] Wong, S. W., K. Wang, Z.-N. Chen, and Q.-X. Chu, "Rotationally symmetric coupled-lines bandpass filter with two transmission zeros," *Progress In Electromagnetics Research*, Vol. 135, 641–656, 2013.

[26] Li, C.-H. and M. Li, "Realization of microstrip bandpass filter balun using double-sided parallel-strip line with novel coupling scheme," *Progress In Electromagnetics Research Letters*, Vol. 43, 191–199, 2013.

[27] Packiaraj, D., K. J. Vinoy, M. Ramesh, and A. T. Kalghatgi, "Design of cascaded three-conductor coupled line filter," *Microwave and Optical Technology Letters*, Vol. 56, No. 10, 2431–2436, 2014.

[28] Kuo, C.-J., C.-Y. Liou, and S.-G. Mao, "Propagation and radiation characteristics of multilayer coupled-line bandpass filters using conductor-backed coplanar transmission lines," *Progress In Electromagnetics Research C*, Vol. 58, 21–31, 2015.

[29] Feng, W. and W. Che, "High-selectivity balanced-filter circuits based on coupled lines with open/shorted loaded stubs," *HKIE Transactions*, Vol. 23, No. 1, 2–11, 2016.

[30] Wu, X., Y. Li, and X. Liu, "High-order dual-port quasi-absorptive microstrip coupled-line bandpass filters," *IEEE Transactions on Microwave Theory and Techniques*, Vol. 68, No. 4, 1462–1475, Apr. 2020.

[31] Salmani, R., A. Bijari, and S. H. Zahiri, "Design of a microstrip dual-band bandpass filter using novel loaded asymmetric two coupled lines for WLAN applications," *Journal of Electrical and Computer Engineering Innovations (JECEI)*, Vol. 8, No. 2, 255–262, 2020.

[32] Yoon, K. and K. Kim, "Compact size of an interdigital bandpass filter with flexible bandwidth and low insertion-loss using a folded spiral and stepped impedance resonant structure," *Electronics*, Vol. 10, No. 16, 2003, Aug. 2021.

[33] Xu, J., K.-D. Xu, M. Zhang, and Q. Chen, "Dual-band bandpass filter using two simple coupled microstrip rings," *Engineering Reports*, Vol. 3, No. 2, e12288, Feb. 2021.

[34] Faisal, M., S. Khalid, M. U. Rehman, and M. A. Rehman, "Synthesis and design of highly selective multi-mode dual-band band-

stop filter," *IEEE Access*, Vol. 9, 43 316–43 323, 2021.

[35] Konpang, J. and N. Wattikornsirikul, "Dual-mode dual-band bandpass filter with high cutoff rejection by using asymmetrical transmission zeros technique," *Progress In Electromagnetics Research M*, Vol. 100, 225–236, 2021.

[36] Wang, P., K. Duan, M. Li, M. Zhang, and B. Jin, "A novel miniaturized l-band filter with great stopband characteristics using interdigitated coupled lines CRLH-TL structure," *Progress In Electromagnetics Research C*, Vol. 114, 57–67, 2021.

[37] Weng, X.-Y., K.-D. Xu, Y.-J. Guo, A.-X. Zhang, and Q. Chen, "High-selectivity bandpass filter based on two merged ring resonators," *Radioengineering*, Vol. 30, No. 3, 504–509, 2021.

[38] Yan, J.-M., Z.-P. Xiao, and L.-Z. Cao, "A simple balanced bandpass filter using loop-type microstrip resonator loaded with shorted/opened stubs," *Progress In Electromagnetics Research Letters*, Vol. 107, 141–149, 2022.

[39] Gruszczynski, S. and K. Wincza, "Extraction of parallel-coupled and end-coupled TEM resonator networks from a coupling matrix in the design of coupled-resonator filters," *Electronics*, Vol. 11, No. 8, 1250, Apr. 2022.

[40] Khani, H. I., A. S. Ezzulddin, and H. Al-Saedi, "Design of high-selectivity compact quad-band BPF using multi-coupled line and short stub-SIR resonators," *Progress In Electromagnetics Research C*, Vol. 122, 215–228, 2022.

[41] Wang, Y. X., W. C. Yang, and M. Jiang, "Bandpass filter design with stub-loaded uniform impedance resonator and L-shaped feed structure," *Progress In Electromagnetics Research Letters*, Vol. 102, 19–26, 2022.

[42] Júnior, J. G. D., J. G. D. Oliveira, V. P. da Silva Neto, and A. G. D'Assunção, "A high-selectivity bandpass filter using dual-mode coupling resonator," *Journal of Microwaves, Optoelectronics and Electromagnetic Applications*, Vol. 21, No. 1, 131–140, 2022.

[43] Ramkumar, S. and R. B. Rani, "Compact reconfigurable bandpass filter using quarter wavelength stubs for ultra-wideband applications," *AEU — International Journal of Electronics and Communications*, Vol. 151, 154219, Jul. 2022.

[44] Wei, G., Y. Wang, J. Liu, and H. Li, "A miniaturized UWB bandpass filter employing multi-stub-loaded short-circuited stepped impedance ring resonator," *Applied Computational Electromagnetics Society Journal (ACES)*, Vol. 38, No. 7, 496–502, Jul. 2023.

[45] Basit, A., A. Daraz, and G. Zhang, "Implementation of a wideband microwave filter design with dual electromagnetic interference (EMI) mitigation for modern wireless communication systems with low insertion loss and high selectivity," *Micromachines*, Vol. 14, No. 11, 1986, 2023.

[46] Shaterian, Z. and M. Mrozowski, "Multifunctional bandpass filter/displacement sensor component," *IEEE Access*, Vol. 11, 27 012–27 019, 2023.

[47] Temuli, H. U. A., K. N. A. Rani, F. A. A. Fuad, K. S. Musa, N. Bahari, F. A. Bakar, M. A. Jamlos, and Y. Rahayu, "Compact parallel coupled line microstrip bpf design for 5G applications," *Journal of Advanced Research in Applied Sciences and Engineering Technology*, Vol. 29, No. 2, 38–52, Jan. 2023.

[48] Fan, X., X. Chen, W. Xu, L. Feng, L. Yu, and H. Yuan, "A filtering switch made by an improved coupled microstrip line," *Applied Sciences*, Vol. 13, No. 13, 7886, Jul. 2023.

[49] Phromloungsri, R., M. Chongcheawchamnan, and S. Sonasang, "Inductively compensated coupled-line resonator and its bandpass filter applications," *Przegląd Elektrotechniczny*, Vol. 99, 55–59, 2023.

[50] Alazemi, A. J., "Dual-band and wideband bandpass filters using coupled lines and tri-stepped impedance stubs," *Micromachines*, Vol. 14, No. 6, 1254, Jun. 2023.

[51] Vryonides, P., S. Arain, A. Quddious, D. Psychogiou, and S. Nikolaou, "A new class of high-selectivity bandpass filters with constant bandwidth and 5:1 bandwidth tuning ratio," *IEEE Access*, Vol. 12, 16 489–16 497, 2024.

[52] Chinda, F. E., M. Hanif, S. Soeung, M. S. Yahya, A. J. A. Al-Gburi, F. Bashir, F. Zahoor, and C. Sovuthy, "Design of sub-6 GHz BPF using chained even and odd mode admittance polynomials for 5G C-band applications," *Results in Engineering*, Vol. 25, 103614, Mar. 2025.

[53] Wu, G., Y. Jin, W. Zhang, R. Jiang, and J. Shi, "Dual band bandpass filters with full band reflectionless response and enhanced upper stopband suppression," *Scientific Reports*, Vol. 15, No. 1, 22520, 2025.

[54] Kahkesh, S. H. and A. Sheikhi, "A microstrip bandpass filter using coupled lines loaded by open stubs," *Scientific Reports*, Vol. 14, No. 1, 26680, 2024.

[55] Li, D., K.-D. Xu, and A. Zhang, "Single-ended and balanced bandpass filters using multiple pairs of coupled lines and stepped-impedance stubs," *IEEE Access*, Vol. 8, 13 541–13 548, 2020.

[56] Shi, J., J. Ren, J. Dong, W. Feng, and Y. Yang, "Supercompact balanced wideband bandpass filter using capacitor-loaded three-line coupled structure," *IEEE Microwave and Wireless Components Letters*, Vol. 32, No. 6, 499–502, 2022.

[57] Xu, K.-D., S. Lu, Y.-J. Guo, and Q. Chen, "Quasi-reflectionless filters using simple coupled line and T-shaped microstrip structures," *IEEE Journal of Radio Frequency Identification*, Vol. 6, 54–63, 2021.

[58] Xu, K.-D., X. Weng, Q. Chen, and H. Fan, "A wideband filtering switch: Its synthesis and design," *IEEE Transactions on Microwave Theory and Techniques*, Vol. 72, No. 1, 43–53, Jan. 2024.

[59] Wu, Q. S., Q. Xue, and C. H. Chan, "Bandpass filter using microstrip ring resonators," *Electronics Letters*, Vol. 39, No. 1, 62–64, Jan. 2003.

[60] Rezaiesarlak, R., F. Hojjat-Kashani, and E. Mehrshahi, "Analysis of capasitively coupled microstrip-ring resonator based on spectral domain method," *Progress In Electromagnetics Research Letters*, Vol. 3, 25–33, 2008.

[61] Jung, D.-J. and K. Chang, "Novel capacitive gap-coupled bandpass filter using non-uniform arbitrary image impedance," *Progress In Electromagnetics Research C*, Vol. 26, 111–121, 2012.

[62] Singh, I. P., P. Bhatt, and A. S. Yadav, "Merits of parallel coupled bandpass filter over end coupled bandpass filter in X band," *International Journal of Electrical, Electronics and Data Communication*, Vol. 3, No. 5, 1–6, 2015.

[63] Kuo, J.-T. and S.-W. Lai, "New dual-band bandpass filter with wide upper rejection band," *Progress In Electromagnetics Research*, Vol. 123, 371–384, 2012.

[64] Xu, X. and W. Wu, "Quasi-elliptic wideband bandpass filters using stubs loaded anti-parallel coupled-line," *Progress In Electromagnetics Research C*, Vol. 42, 13–28, 2013.

[65] Cabello-Sánchez, J., V. Drakinskiy, J. Stake, and H. Rodilla, "Capacitively-coupled resonators for terahertz planar-Goubau-line filters," *IEEE Transactions on Terahertz Science and Technology*, Vol. 13, No. 1, 58–66, Jan. 2023.

[66] Pozar, D. M., *Microwave Engineering*, 4th ed., Wiley, 2012.

[67] Priyanka, P. and S. Maheswari, "Design of microstrip coupled line bandpass filter using synthesis technique," *International*

Journal of Engineering Research & Technology (IJERT), Vol. 6, No. 2, 2018.

[68] Liu, H., X. Li, Y. Guo, S.-J. Fang, and Z. Wang, "Design of filtering coupled-line trans-directional coupler with broadband bandpass response," *Progress In Electromagnetics Research M*, Vol. 100, 163–173, 2021.

[69] Balanis, C. A., *Antenna Theory: Analysis and Design*, John Wiley & Sons, 2016.

[70] Cui, J., H. Chang, and R. Zhang, "High selectivity slot-coupled bandpass filter using discriminating coupling and source-load coupling," *Applied Sciences*, Vol. 10, No. 19, 6807, 2020.